Available online at www.sciencedirect.com

ScienceDirect

Ceramics International 35 (2009) 2373–2380

CERAMICS INTERNATIONAL

www.elsevier.com/locate/ceramint

Mechanical characteristics of porous hydroxyapatite/oxide composites produced by post-sintering hot isostatic pressing

M.A. Auger [a], B. Savoini [a], A. Muñoz [a], T. Leguey [a], M.A. Monge [a,*],
R. Pareja [a], J. Victoria [b]

[a] Departamento de Física, Universidad Carlos III de Madrid, Avd. Universidad 30, 28911 Leganés, Madrid, Spain
[b] Departamento de Física, Universidad de Las Palmas de Gran Canaria, Tafira Baja, Las Palmas de Gran Canaria, Spain

Received 5 January 2009; received in revised form 9 January 2009; accepted 29 January 2009

Abstract

Porous hydroxyapatite and hydroxyapatite/oxide composites, with 10 wt% addition of Y_2O_3, ZrO_2 or TiO_2 have been prepared by hot isostatic pressing after pressureless sintering, and their phase composition, mechanical properties and microstructure investigated. The quantitative X-ray diffraction analyses reveal that the addition of Y_2O_3 inhibits the hydroxyapatite decomposition completely during the consolidation processes as a result of the Y ion dissolution into the hydroxyapatite lattice. On the contrary, it is found that the addition of ZrO_2 or TiO_2 enhances the decomposition of hydroxyapatite into $Ca_3(PO_4)_2$, which causes the transformation of the starting oxides. The mechanical characterization of the materials has been accomplished by three-point flexure tests, and nanoindentation and microhardness measurements. Post-sintering hot isostatic pressed pure hydroxyapatite, which resulted in a porous biphasic material with 13.2 wt% β-$Ca_3(PO_4)_2$, exhibited the best mechanical properties. The failure of hydroxyapatite-10Y_2O_3 during the flexure tests was no catastrophic in contrast to the catastrophic behaviour found in the other materials.

Keywords: A. Hot isostatic pressing; Hydroxyapatite; Biomaterials

1. Introduction

Hydroxyapatite (HA), $Ca_{10}(PO_4)_6(OH)_2$, should be the most appropriate material for hard tissue replacement implants since it is the inorganic structural constituent of bones and teeth, has an excellent bone-bonding capability and is highly bioactive and biocompatible [1]. However, HA is restricted to non load-bearing applications because of its inherent brittleness. For load-bearing implants, metals and ceramics with a good biocompatibility, such as Ti alloys, ZrO_2 and TiO_2, are used. These implants may induce clinical problems because these materials lack bioactivity to promote bonding to the surrounding tissues and have a higher stiffness than the bone. Presently, composites formed by HA and ceramic oxides are being investigated to develop bioceramic materials with improved bioactivity and mechanical properties. These composites are produced by sintering of synthetic HA and a biocompatible oxide, usually yttria-stabilized ZrO_2 (YSZ) [2–6]; also, other oxides such as Al_2O_3 and TiO_2 have been used [7–9]. Some of these composites appear to exhibit improved strength and fracture toughness increasing the oxide fraction but simultaneously their bioactivity is reduced compared to pure HA [2,10–13]. These oxides promote the HA decomposition during pressureless sintering giving rise to tricalcium phosphate $Ca_3(PO_4)_2$ (TCP), and other deleterious secondary phases that preclude densification of HA-oxide composites and degrade their characteristics. Thus, a suitable balance between mechanical properties and bioactivity of these biocomposites is presently explored through lowering the oxide fraction, using reinforcement phases that inhibit the HA decomposition during processing.

The purpose of the present investigation is to survey the capability of Y_2O_3 to inhibit the HA degradation during the fabrication process of a porous HA/Y_2O_3 composite, and asses its mechanical properties in comparison to identically processed HA/ZrO_2 and HA/TiO_2 composites. With this aim,

---

* Corresponding author. Tel.: +34 916249414; fax: +34 916248749.
E-mail address: mmonge@fis.uc3m.es (M.A. Monge).

0272-8842/$34.00 © 2009 Elsevier Ltd and Techna Group S.r.l. All rights reserved.
doi:10.1016/j.ceramint.2009.01.016

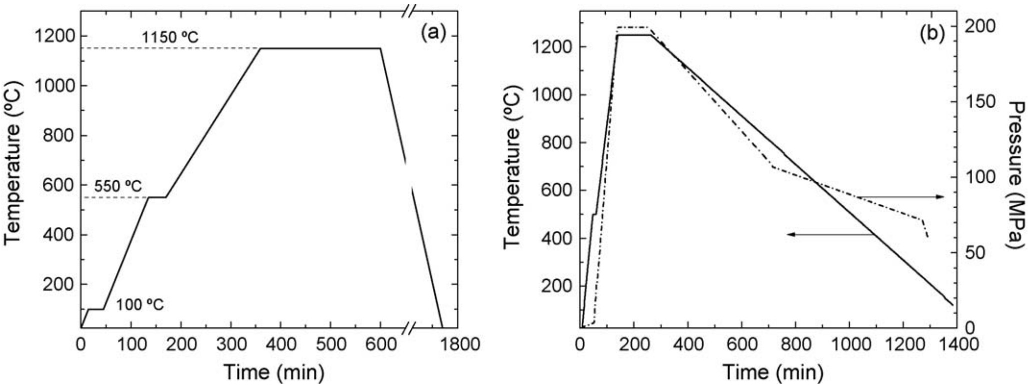

Fig. 1. (a) Pressureless sintering and (b) HIP cycles used to produce porous bulk HA and HA-oxide composites.

pure HA and HA composites with 10 wt% of Y_2O_3, ZrO_2 and TiO_2 have been prepared by hot isostatic pressing after pressureless sintering in air (post-sintering HIP).

HIP post-sintering treatments can improve the mechanical properties of HA-based materials since they can reduce close porosity and prevent the decomposition reactions of HA that degrade the mechanical strength of the HA-based materials [14,15]. YSZ, i.e. tetragonal ZrO_2 (t-ZrO_2), appears to be the reinforcement phase that yields the best mechanical behaviour in HA-based composites [16,17], but it does not enhance their bioactivity [11,12]. TiO_2 has been added to HA to produce materials with enhanced bioactivity, but neither the mechanical properties nor the bioactivity of the composite materials are meaningfully improved [9,18]. However, Y appears to be a Ca substitute in the HA lattice that enhances the bioactivity of HA. It has been reported that Y-doped HA has the capability to improve the osteoblast function over pure HA and other HA-based composites [19–21]. Nevertheless, the mechanical and compositional characteristics of HA/Y_2O_3 composites seem not to have been reported before. Other reasons to investigate their properties is the interest arisen by the interaction between Y_2O_3 and HA due to the potential of Y_2O_3 as a medium to compose functional HA. Eu^{3+}-doped Y_2O_3 nanoparticles act as nanophosphors when they are coating HA particles, but their luminescent capability disappears in absence of the HA substrate [22]. This behaviour has been attributed to diffusion of ions across the HA/Y_2O_3 interface or structural distortion of the Y_2O_3 lattice. Also, HA/Y_2O_3 might be a suitable vehicle for selective internal radioimmunotherapy with ^{90}Y.

2. Experimental procedure and method

The starting materials were: high purity synthetic HA, BABI-HAP-P mesh-100, supplied by Berkeley Advanced Biomaterials; nanometric powders of TiO_2 (rutile) with an average particle size of 29 nm, and monoclinic Y_2O_3 with particle sizes $\leq$50 nm, both from Nanophase Technologies; and 99.9% pure YSZ (ZrO_2—7.9 mol% Y_2O_3) from Aldrich with an average particle size of 0.25 μm. Powders with compositions, HA-10 wt% Y_2O_3, HA-10 wt% ZrO_2 and HA-10 wt% TiO_2 were blended for 2 h in a Turbula® mixer. The blends, as well as pure HA, were compacted in silicone moulds by cold isostatic pressing (CIP), maintaining a pressure of 250 MPa for 2 min. After CIP, green compacts with dimensions ~7 mm Ø and ~50 mm length and ~12 mm × 12 mm × 55 mm were obtained. These compacts were pressureless sintered at 1150 °C for 4 h in air, and then subjected to hot isostatic pressing (HIP) for 2 h at 1250 °C and in pure Ar atmosphere at 190 MPa. Fig. 1 shows the sintering and HIP cycles applied. A cooling rate of less than 2 °C/min was used to prevent the appearance of cracks due to differences in the thermal expansion coefficient of the phases, which could form during sintering.

X-ray diffraction (XRD) measurements were carried in an X-Pert Philips diffractometer using the Cu Kα radiation. The diffraction patterns were recorded from 10° to 100° in 2θ in steps of 0.01° with counting times of 5 s. The phases present in the materials were identified from the quantitative analyses of the XRD patterns using the Rietveld method, the FULLPROF software, and the crystallographic data from the reference JCPDS files [23,24]. Scanning electron microscopy (SEM) and energy dispersive spectroscopy (EDS) analyses were carried out in a Philips XL-30 or JEOL JSM6500f microscope equipped with energy dispersive X-ray spectrometers.

After each consolidation stage, the apparent density of the materials was calculated as m/V, where m is the sample mass and V the volume determined from the sample dimensions. In addition, precise density measurements of the HIP post-sintered samples were carried out in a He ultrapycnometer in order to determine their open porosity. The total porosity of the HIP post-sintered materials was determined as $P = (1 - \rho'_{\rm h}/\rho_{\rm th})$ and the open porosity as $P_{\rm o} = (1 - \rho'_{\rm h}/\rho_{\rm He})$. $\rho'_{\rm h}$, $\rho_{\rm He}$ and $\rho_{\rm th}$ are the apparent density, the density measured in the He ultrapycnometer and the theoretical density calculated for each material applying the mixture rule to the phase composition obtained from the XRD analyses.

The mechanical characterization of the samples was performed by means of micro- and nanohardness measurements, and flexure tests. The Vickers microhardness measurements were made applying a load of 9.8 N for 20 s in a TIME Technology Europe HSC-1000 tester. Nanoindentation measurements were carried out in a Nanoindenter IIs MTS. The

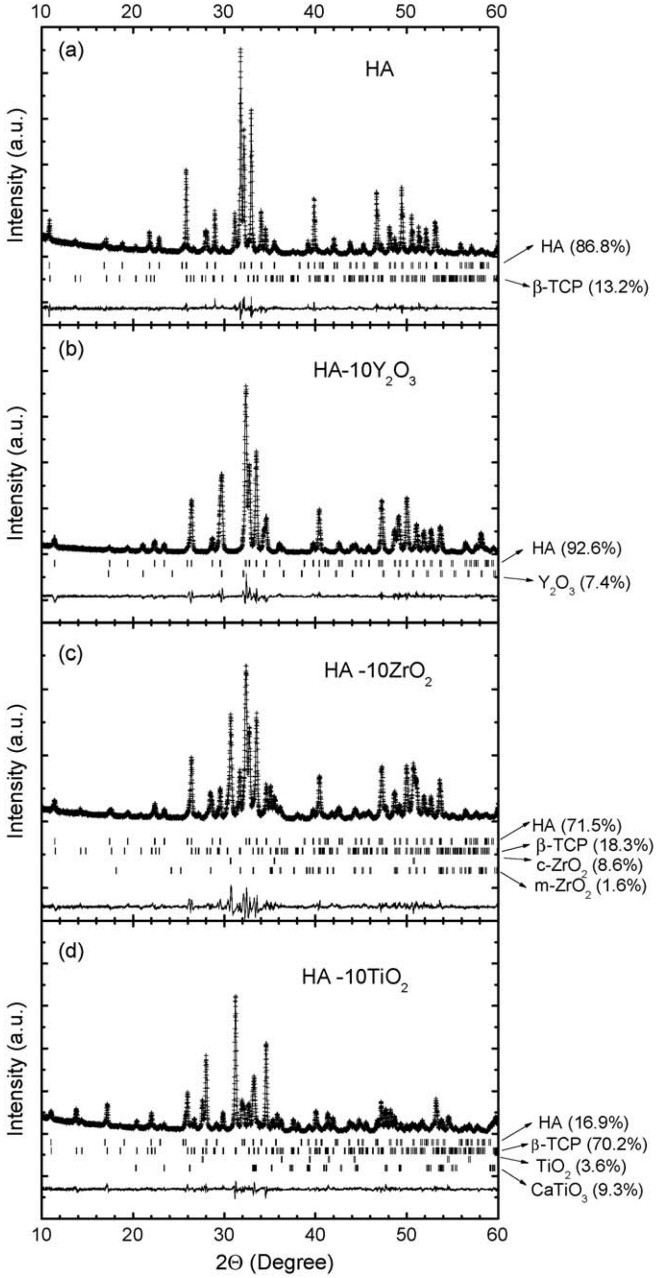

Fig. 2. Experimental XRD patterns fitted by FULLPROF for HIP post-sintered samples: (a) HA; (b) HA-10Y_2O_3; (c) HA-10ZrO_2; (d) HA-10TiO_2. The theoretical positions of the diffraction peaks corresponding to the phases detected in the samples are represented below the diffraction patterns, along with the phase composition obtained from the quantitative analyses, and the deviation between the experimental and adjusted patterns. The phase composition in weight fractions is given in parentheses.

distance between two consecutive indentations was 50 μm, and the maximum applied load 250 mN. The elastic modulus was determined from the load–displacement curves during unloading. Three-point flexure tests were performed on ~22 mm × 3 mm × 3 mm samples using a span of 16 mm and a cross-head rate of 0.2 mm/min. The flexural elastic modulus and strength were determined from the load–displacement curves.

Table 1

Densities determined after each consolidation stage and final porosities after post-sintering HIP treatment at 1250 °C. ρ'_g, ρ'_s and ρ'_h are the apparent densities measured from the dimensions and weights of the samples after: CIP, sintering at 1150 °C and subsequent HIP at 1250 °C, respectively. ρ_{He} is the density measured in a He ultrapycnometer and ρ_{th} the theoretical density. P and P_o are the total and open porosities, respectively.

Sample	ρ'_g	ρ'_s	ρ'_h	ρ_{He}	ρ_{th}	P	P_o
HA	1.85	1.98	2.24	2.954	3.14	0.29	0.24
HA-10Y_2O_3	1.87	2.12	2.37	3.211	3.25	0.27	0.26
HA-10ZrO_2	1.89	2.11	2.42	3.223	3.30	0.27	0.25
HA-10TiO_2	1.84	2.07	2.04	3.117	3.19	0.36	0.35

3. Results and discussion

3.1. Density measurements

The apparent density of the materials after each consolidation stage is given in Table 1, along with their total and open porosity after the HIP treatment. It is found that after pressureless sintering at 1150 °C the porosity, defined by $(1-\rho'_s/\rho_{th})$, is ~0.35 irrespective of the material. This high porosity would annul the pressure effect on sintering power of the subsequent HIP at 1250 °C. However, it produced further densification with the exception of HA-10TiO_2 that did not change its apparent density meaningfully. This suggests that, in addition to sintering, HA decomposition and reactions with the reinforcement phase would continue during the subsequent HIP.

3.2. XRD measurements

Fig. 2 shows the experimental XRD patterns fitted by FULLPROF for the post-sintering HIP treated samples. In addition, the theoretical position of the characteristic diffraction peaks of the phases detected in each sample and the corresponding phase composition in weight is shown in Fig. 2. The hexagonal lattice parameters of the HA phase in each sample and its unit cell volume are given in Table 2. The XRD measurements indicated that the pure HA sample after the post-sintering HIP treatment was transformed into a biphasic material composed of HA and 13.2 wt% β-TCP; no other phases were detected. The XRD pattern of the as-received pure HA powder only showed presence of HA phase. A precise fit of this XRD pattern using FULLPROF was attained assuming OH^- and Ca^{2+} default in the HA lattice. From the quantitative analyses of the XRD pattern of post-sintering HIP treated HA, according to the method described in Ref. [25], an accurate

Table 2

Hexagonal lattice parameters and unit cell volume for the HA phase in the as-received HA powder and in the post-sintering HIP treated samples.

Sample	a (Å)	Δa (Å)	c (Å)	Δc (Å)	V (Å^3)	ΔV (Å^3)
As-received HA	9.415	–	6.884	–	1585.4	–
HA	9.411	−0.004	6.896	0.012	1586.6	1.2
HA-10Y_2O_3	9.425	0.010	6.900	0.016	1592.4	7.0
HA-10ZrO_2	9.428	0.013	6.909	0.025	1595.6	10.2
HA-10TiO_2	9.408	−0.007	6.958	0.074	1560.0	−25.4

Ca/P ratio in the starting HA powder can be obtained from the following formula:

$$\frac{\mathrm{Ca}}{\mathrm{P}} = \frac{(10 f_{\mathrm{HA}}/M_{\mathrm{HA}}) + (3 f_{\mathrm{TCP}}/M_{\mathrm{TCP}})}{(6 f_{\mathrm{HA}}/M_{\mathrm{HA}}) + (2 f_{\mathrm{TCP}}/M_{\mathrm{TCP}})} \quad (1)$$

where f_{HA} and f_{TCP} represent the weight fraction of HA and TCP, $f_{\mathrm{HA}} + f_{\mathrm{TCP}} = 1$, and M_{HA} and M_{TCP} the corresponding molar weights. A Ca/P ratio of 1.642 was obtained.

Post-sintering HIP treated HA-10Y_2O_3 showed no evidence for new phases produced by HA decomposition or reaction with Y_2O_3 during the consolidation treatments. The detection limit of the diffractometer is estimated to be less of ~0.5 wt% for any other secondary phase. Nevertheless, the starting Y_2O_3 fraction decreased to 7.4 wt% indicating that some reaction did take place between HA and Y_2O_3. The most plausible reaction is the dissolution of Y^{3+} ions into the HA lattice, with the subsequent suppression of the HA decomposition into β-TCP under the present consolidation treatments. Assuming that all the Y^{3+} ions corresponding to the 2.6 wt% Y_2O_3 loss were dissolved into the HA lattice occupying Ca vacancy sites, the expected (Ca + Y)/P ratio would be 1.665, in fact very close to the stoichiometric one 1.667.

The XRD results for HA-10ZrO_2 and HA-TiO_2 evidenced the HA decomposition in β-TCP and formation of other phases during the consolidation treatments. The total amount of ZrO_2 in HA-10ZrO_2 remained virtually constant upon the consolidation treatments, but the starting tetragonal phase of YSZ was completely transformed into cubic and monoclinic phases, resulting in total phase compositions of 8.6 wt% c-ZrO_2, and 1.6 wt% m-ZrO_2. XRD measurements performed on the starting 7.9 mol% YSZ powder revealed that it indeed consisted of t-ZrO_2 with <1 wt% m-ZrO_2. Then, the consolidation treatments destabilized the t-ZrO_2 phase suppressing the potential toughening capability of the YSZ addition.

In HA-TiO_2 the HA decomposition was very extensive, yielding 9.3 wt% $CaTiO_3$ as a result of the reaction of CaO with the reinforcement phase TiO_2, CaO being produced by the HA → TCP transformation. In this case, the β-TCP fraction resulted in 70.2 wt%, which is much higher than the corresponding ones in HA and HA-10ZrO_2.

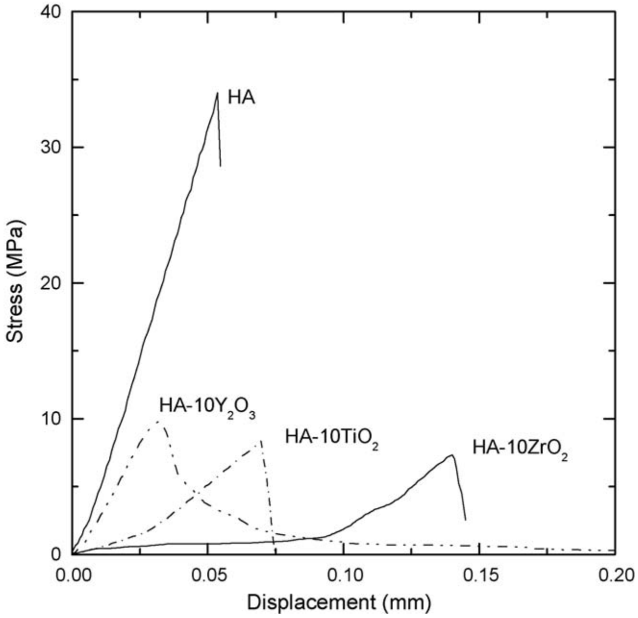

Fig. 3. Representative flexural stress–displacement curves for HA and HA-oxide composites obtained from three-point tests.

3.3. Mechanical characterization

3.3.1. Flexure tests

Fig. 3 shows representative stress–displacement curves of the post-sintering HIP treated materials obtained from the three-point flexure tests. Their mechanical characteristics are summarized in Table 3 along with the densification ratio defined as $1 - P$. The flexural characteristics: strength σ_{f}, flexural modulus E_{f} and work of fracture w_{f} are average values from six flexure tests. The fracture toughness K_{IC} can be estimated applying the lineal elastic approach through the equation [26]:

$$G_{\mathrm{IC}} = \frac{K_{\mathrm{IC}}^2}{E} \quad (2)$$

where E is the elastic modulus, and G_{IC} the energy release rate at fracture, which would be equivalent to the work of fracture w_{f} obtained from the flexure tests. The elastic modulus values E_{f} obtained from the flexure tests, or E obtained from the nanoindentation measurements, were used to estimate the K_{IC} values. These values are given in Table 3.

The results indicate that neither the phase composition of the materials nor their densification ratio appear to be the specific parameters determining the mechanical characteristics of the present HA materials. For instance, the best mechanical properties: $\sigma_{\mathrm{f}} = 35$ MPa and $K_{\mathrm{IC}} \cong 2.5$ MPa, corresponded to post-sintering HIP treated HA samples which were a biphasic material with composition HA-13.2 wt% β-TCP and a

Table 3
Mechanical characteristics of the post-sintering HIP treated samples. E_{f} and E values are determined from the flexure curves and from nanoindentation measurements, respectively, and the densification ratio is defined as $1 - P$.

Sample	Flexural strength (MPa)	Flexural modulus, E_{f} (GPa)	Fracture work, w_{f} (J/m^2)	Fracture toughness, K_{IC} (MPa m$^{1/2}$)	Nanohardness, NH (GPa)	E modulus (GPa)	Fracture toughness, K_{IC} (MPa m$^{1/2}$)	Vickers microhardness, HV (GPa)	Densification ratio
HA	35 ± 4	66 ± 15	93 ± 30	2.5	1.7 ± 0.2	62 ± 5	2.4	1.78 ± 0.02	0.71
HA-10Y_2O_3	8 ± 5	22 ± 13	17 ± 8	0.6	1.8 ± 0.2	55 ± 2	1.0	1.08 ± 0.01	0.73
HA-10ZrO_2	8 ± 3	21 ± 15	64 ± 40	1.2	1.7 ± 0.1	59 ± 3	1.9	1.09 ± 0.01	0.73
HA-10TiO_2	16 ± 5	11 ± 2	37 ± 10	0.6	0.8 ± 0.1	51 ± 2	1.4	1.00 ± 0.01	0.64

densification ratio of 0.71. The worst properties corresponded to HA-10Y_2O_3, which also gave rise to a biphasic material with composition HA-7.4 wt% Y_2O_3, without any evidence for TCP, and a densification ratio of 0.73. Although Y_2O_3 inhibit the HA → TCP transformation, the resulting material is not strengthened and its toughness is the lowest. However, it is worth to notice that the flexure curves for HA-10Y_2O_3 were qualitatively different from those for HA-13.2 wt% TCP and the other materials. HA-10Y_2O_3 samples exhibited no catastrophic failure characterized by a very slow decrease of the load after attaining a point of maximum load. This is in contrast with the brittle behaviour found for HA-13.2 wt% TCP and the other materials, which fracture catastrophically before attaining a maximum load point. Thus, some toughening mechanism appears to act in HA-10Y_2O_3.

HA-10ZrO_2 and HA-10TiO_2 having a four-phase composition apparently exhibited mechanical properties similar to those of biphasic HA-10Y_2O_3. However, HA-10ZrO_2 samples tended to yield higher work of fracture and toughness in comparison to HA-10Y_2O_3 and HA-10TiO_2, see Table 3. It should be noted that the flexure curves for HA-10ZrO_2 exhibited two distinctive stages of deformation. An initial lineal stage with a very low increase rate that was extended up to between ~40% and 75% of the fracture strain, is followed by a faster second stage up to fracture. Similarly two-stage behaviour in pure HA with porosity ~40% has been attributed to pore closing during the initial stage of deformation [27]. This two-stage behaviour in the flexure curves of the other materials, if there exists, is irrelevant to extract conclusions. However, these materials had porosity values equal or slightly higher than HA-10ZrO_2. All the above suggests that porosity itself cannot be responsible for the two-stage hardening found in HA-10ZrO_2.

The K_{IC} values obtained in the pure HA samples are similar to those reported for dense HA but higher than the reported values for porous HA [1,15,28]. Also, the K_{IC} values found for the HA-oxide composites are similar or slightly smaller than the values reported for dense HA-ZrO_2 composites [1,15]. When K_{IC} values are compared, it should be noticed that the fracture toughness is quite sensitive to the measurement methods, and the K_{IC} values reported for HA in the literature have usually been determined from hardness tests.

3.3.2. Nanoindentation and Vickers microhardness tests

The matrix nanohardness and elastic modulus measured at a contact depth of 2200 nm are summarized in Table 3. These values for HA-10TiO_2 resulted in values noticeably smaller than those for the other materials. It appears that these discrepancies are due to the matrix composition, i.e. 100% HA in HA-10Y_2O_3, HA/(13–20) wt% β-TCP in HA and HA-10ZrO_2, but 81 wt% β-TCP/19 wt% HA in HA-10TiO_2. E values in the range 60–80 GPa have also been reported for porous HA with densities between 2.3 and 2.6 g/cm^3 [29].

The microhardness and nanohardness values of the HA samples agreed, but differed noticeably in the case of the HA-oxide composites. The oxide dispersion in the present conditions appeared to have no hardening effect on the matrix of HA-TCP or HA.

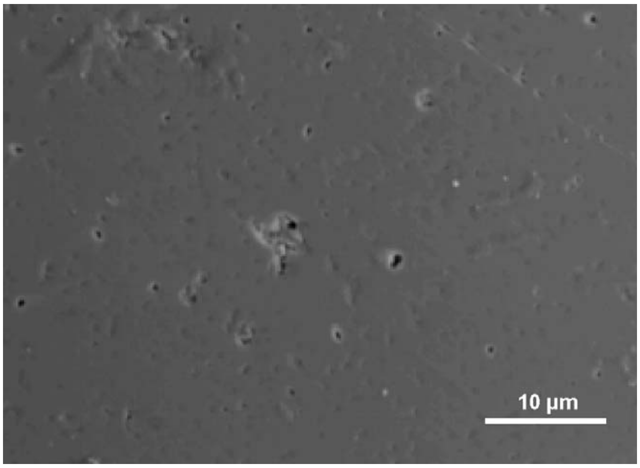

Fig. 4. SEM image of post-sintering HIP treated HA.

3.4. Microstructure and fracture

A typical microstructure exhibited by the surfaces of the investigated materials after being mechanically polished is as shown in Figs. 4 and 5. The SEM images of the surfaces did not appear to reflect the true porosity and pore shape of the

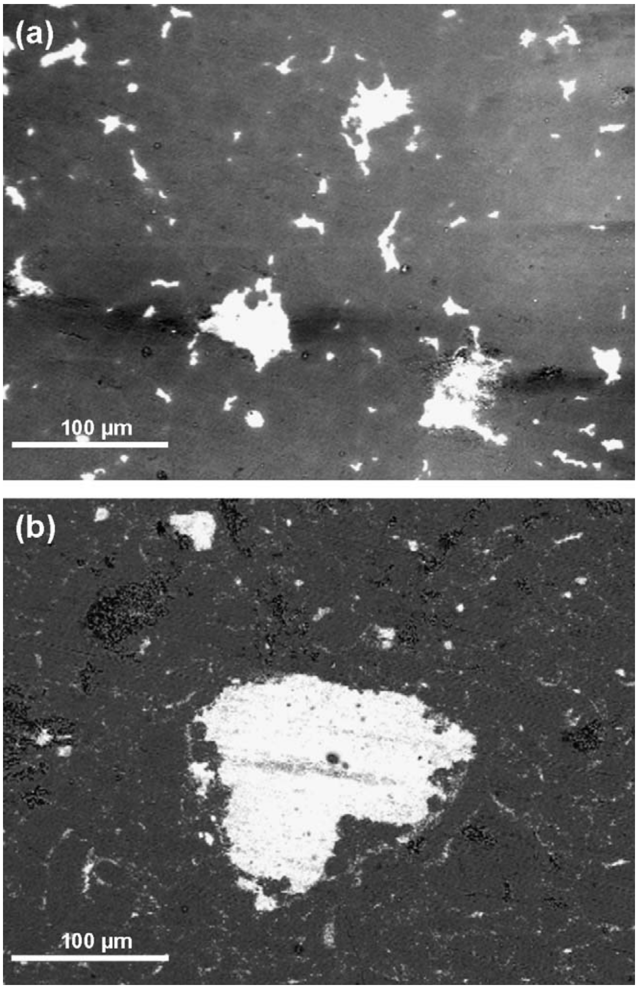

Fig. 5. BSE images of post-sintering HIP treated samples of (a) HA-10Y_2O_3 and (b) HA-10ZrO_2.

materials since the observed porosity agreed neither with those determined from density measurements nor with the ones observed in the unpolished fracture surfaces. The samples containing oxide particles showed inhomogeneous distribution of particle size. Very large particles, produced by either HA decomposition reaction and/or inappropriate dispersion of the starting oxides by mechanical mixing, are found. In the case of HA-10ZrO_2, small ZrO_2 particles appeared decorating the borders of previous agglomerates of HA particles and/or grain boundaries, as Fig. 5b shows. This was not evident in HA-10Y_2O_3 and HA-10TiO_2. However, in HA-10Y_2O_3, element map images obtained from EDS analyses revealed that Y was also homogeneously distributed in the matrix, as Fig. 6 shows. This confirms the XRD results that indicate the Y intake into the HA lattice.

Fig. 7 shows the fracture surface for an HA sample. The surface was rough and had a flaky appearance. Now, the porosity is evident, as well as a second phase with a dark contrast associated to the pores, as the backscattered electron image reveals. This second phase having less density than the HA matrix should be β-TCP detected by XRD.

The fracture surface of the materials containing Y_2O_3 or ZrO_2 also showed porosity and flaky appearance when observed under high magnification. However, low magnification images revealed fracture surfaces having a polyhedral relief with apparently flat facets, abundant branching of secondary cracks and large oxide particles on the facets, as Figs. 8 and 9 show. This indicates that the crack propagation occurs between HA

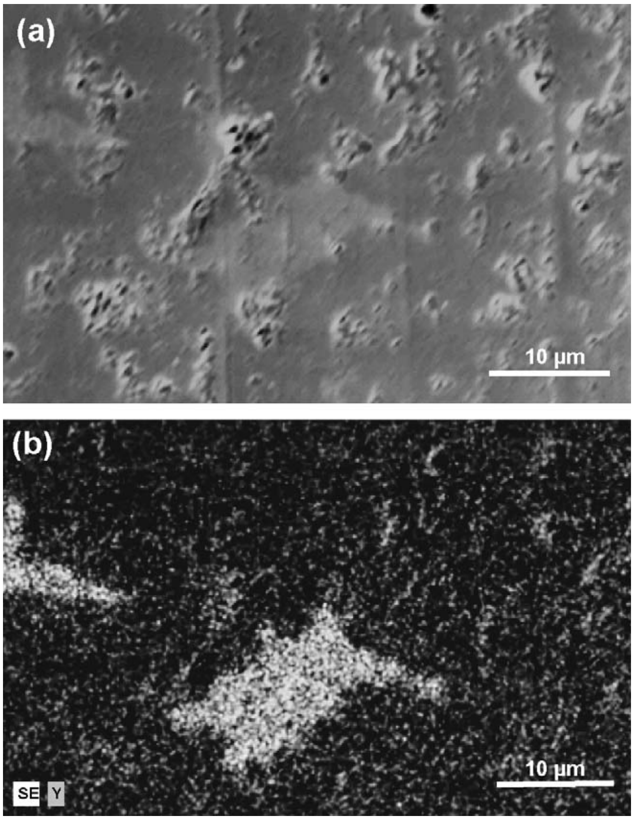

Fig. 6. Post-sintering HIP treated HA-10Y_2O_3. (a) SE image showing large Y_2O_3 particles, and (b) its element map of the Y distribution.

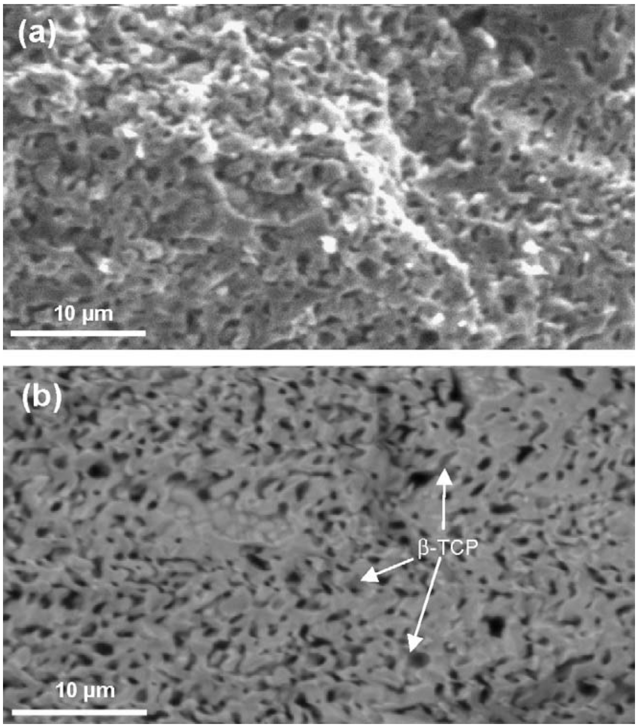

Fig. 7. (a) SE and (b) BSE images of the fracture surface of post-sintering HIP treated HA.

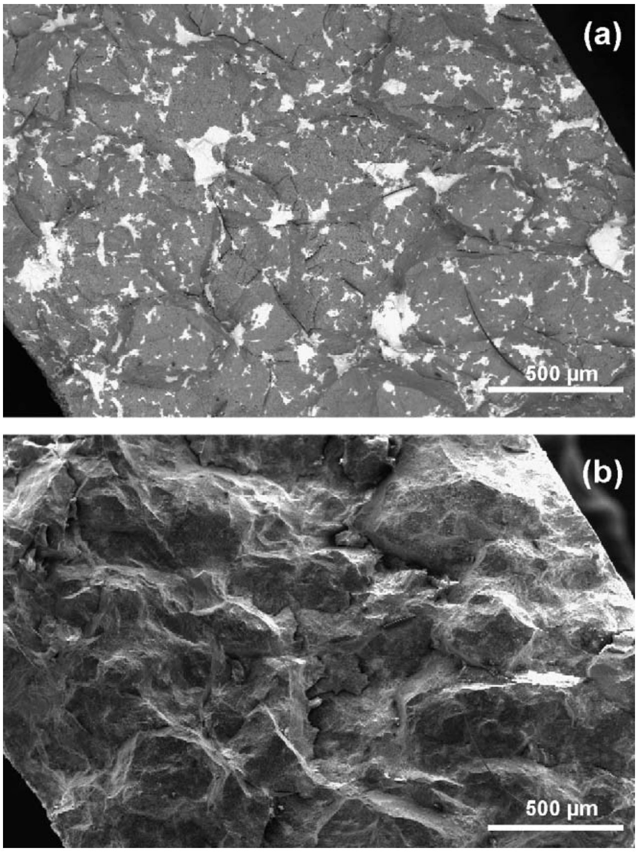

Fig. 8. Fracture surface of post-sintering HIP treated HA-10Y_2O_3. (a) BSE image showing the distribution of Y_2O_3 (bright areas) and cracks; (b) SE image showing the surface relief.

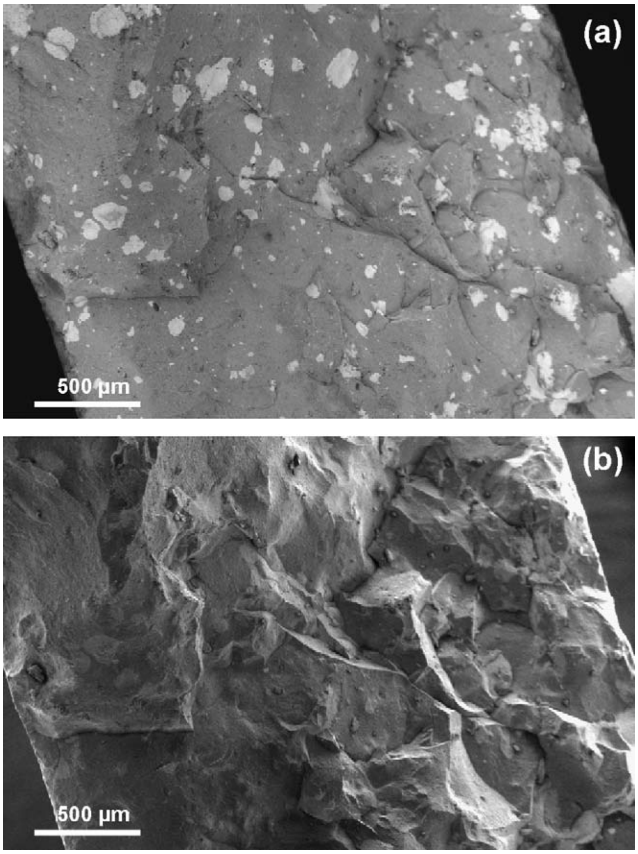

Fig. 9. Fracture surface of post-sintering HIP treated HA-10ZrO_2. (a) BSE image showing the distribution of ZrO_2 (bright areas) and cracks; (b) SE image showing the surface relief.

grain boundaries or previous agglomerates of HA particles, i.e. the fracture mode is intergranular. Thus, the decrease of the flexural strength and fracture toughness in HA-oxide materials relative to the HA samples may be attributed to a reduction of the cohesion energy between the HA grains and agglomerates due to setting of oxide particles at these boundaries. It should be noted the distinctive morphology of the large Y_2O_3 particles in HA-10Y_2O_3 compared to the corresponding one to ZrO_2 in HA-10ZrO_2, see Figs. 8 and 9. Y_2O_3 particles have a very irregular shape in contrast to ZrO_2 particles, which are round. In principle, no other distinctive characteristics in the fracture surface of HA-10Y_2O_3 were observed, to account for its no catastrophic failure exhibited in the flexure tests in comparison with HA-10ZrO_2. However, thorough examination of the crack trails shows that the oxide particles, in addition to deflect the cracks or be broken, might also act as bridging ligaments when propagating cracks run into some of the oxide particles, see Fig. 10. Although these bridging events were not profusely found, under the observation conditions used in examined HA-10Y_2O_3, they might have enough toughening effect to induce no catastrophic failure in this material.

The characteristics of the fracture surface in HA-10TiO_2 are clearly different from the above, as Fig. 11 shows. Secondary cracks perpendicular to the fracture surface, crack branching and facets, did not appear profusely but localized in the $CaTiO_3$ large particles formed by the HA decomposition reactions, and in the surrounding matrix. These observations suggest that fracture in HA-10TiO_2 initiated in these particles, and the crack propagation is mainly porosity controlled.

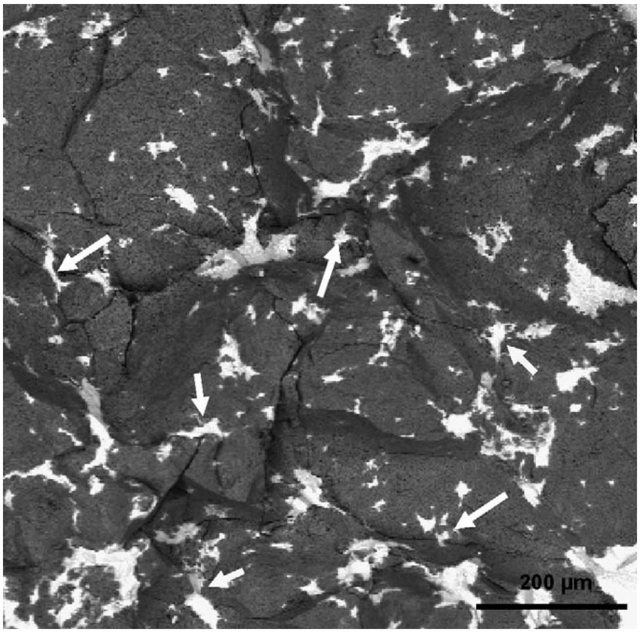

Fig. 10. Details of the crack–particle interaction suggesting particle bridging in HA-10Y_2O_3.

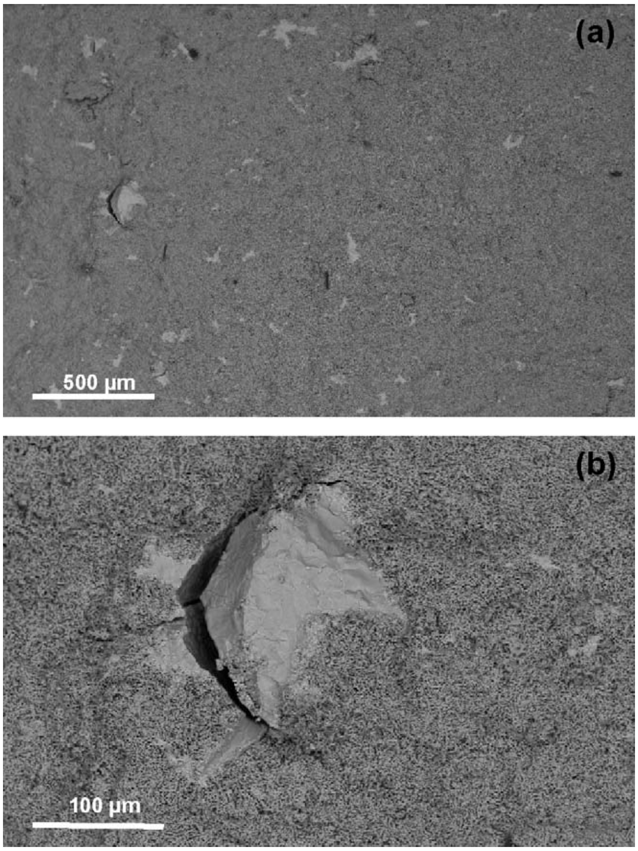

Fig. 11. BSE images showing the distribution of $CaTiO_3$ and TiO_2, and secondary cracks in the fracture surface of HA-10TiO_2.

4. Conclusions

Materials prepared by post-sintering HIP treatments of pure HA or HA containing 10 wt% of Y_2O_3, t-ZrO_2 or TiO_2 particles resulted in porous composites with open porosities between 0.35 and 0.24. The Y_2O_3 addition inhibited the HA decomposition into TCP completely producing a biphasic composite with composition HA-7.3 wt% Y_2O_3. The quantitative XRD analyses show that Y ions from the starting Y_2O_3 dissolved into the HA lattice occupying Ca positions. However, the t-ZrO_2 or TiO_2 addition increased the HA decomposition into TCP, which produced the transformation of these starting oxides.

The HA-13.2 wt% β-TCP composite produced by post-sintered HIP of pure HA exhibited the best mechanical characteristics. The flexure tests and the microhardness measurements indicate that the oxide dispersion produced under the present consolidation treatments do not improve the mechanical characteristics in comparison with the composite produced from pure HA. However, HA-10Y_2O_3 exhibited no catastrophic failure during the flexure tests in contrast to the catastrophic behaviour of the other composites. The SEM observations indicate that particle bridging might be responsible for the no catastrophic behaviour of HA-10Y_2O_3.

Acknowledgements

The authors gratefully acknowledge the financial support from the Comunidad de Madrid and the Ministry of Education and Science of Spain, through the programs ESTRUMAT-CM (MAT/77) and Juan de la Cierva, respectively.

References

[1] W. Suchanek, M. Yoshimura, J. Mater. Res. 13 (1998) 94–117.
[2] J. Li, H. Liao, L. Hermansson, Biomaterials 17 (1996) 1787–1790.
[3] R.B. Heimann, T.A. Vu, J. Mater. Sci. Lett. 16 (1997) 437–439.
[4] Z.J. Shen, E. Adolfsson, M. Nygren, L. Gao, H. Kawaoka, K. Niihara, Adv. Mater. 13 (2001) 214–216.
[5] Z. Evis, C. Ergun, R.H. Doremus, J. Mater. Sci. 40 (2005) 1127–1134.
[6] Z. Evis, Ceram. Int. 33 (2007) 987–991.
[7] J. Li, B. Fartash, L. Hermansson, Biomaterials 16 (1995) 417–422.
[8] T.A. Vu, R.B. Heimann, J. Mater. Sci. Lett. 16 (1997) 1680–1682.
[9] F.N. Oktar, Mater. Lett. 60 (2006) 2207–2210.
[10] H.W. Kim, Y.J. Noh, Y.H. Koh, H.E. Kim, H.M. Kim, Biomaterials 23 (2002) 4113–4121.
[11] T.M. Lee, R.S. Tsai, E. Chang, C.Y. Yang, M.R. Yang, J. Mater. Sci.: Mater. Med. 13 (2002) 281–287.
[12] T.M. Lee, C.Y. Yang, E. Chang, R.S. Tsai, J. Biomed. Mater. Res. 71A (2004) 652–660.
[13] Z. Evis, M. Sato, T.J. Webster, J. Biomed. Mater. Res. 78A (2006) 500–507.
[14] K. Ioku, M. Yoshimura, S. Somiya, Biomaterials 11 (1990) 57–61.
[15] K. Ioku, S. Somiya, M. Yoshimura, J. Ceram. Soc. Jpn. 99 (1991) 196–203.
[16] Z. Evis, R.H. Doremus, J. Mater. Sci. 42 (2007) 2426–2431.
[17] K.A. Khalil, S.W. Kim, H.Y. Kim, Mater. Sci. Eng. A 456 (2007) 368–372.
[18] P.A. Ramires, A. Romito, F. Cosentino, E. Milella, Biomaterials 22 (2001) 1467–1474.
[19] T.J. Webster, C. Ergun, R.H. Doremus, R. Bizios, J. Biomed. Mater. Res. 59 (2002) 312–317.
[20] T.J. Webster, E.A. Massa-Schlueter, J.L. Smith, E.B. Slamovich, Biomaterials 25 (2004) 2111–2121.
[21] M. Sato, M.A. Sambito, A. Aslani, N.M. Kalkhoran, E.B. Slamovich, T.J. Webster, Biomaterials 27 (2006) 2358–2369.
[22] W. Wang, D. Shi, J. Lian, Y. Guo, G. Liu, L. Wang, R.C. Ewing, Appl. Phys. Lett. 89 (2006) 183106.
[23] H.M. Rietveld, J. Appl. Crystallogr. 2 (1969) 65–71.
[24] J. Rodriguez-Carvajal, Physica B 192 (1993) 55–69.
[25] S. Raynaud, E. Champion, D. Bernache-assollant, J.P. Laval, J. Am. Ceram. Soc. 84 (2001) 359.
[26] T.L. Anderson, Fracture Mechanics. Fundamentals and Applications, 2nd ed., CRC Press, Boca Raton, FL, USA, 1995 (Chapter 2).
[27] S. Pramanik, A.K. Agarwal, K.N. Rai, A. Garg, Ceram. Int. 33 (2007) 419.
[28] S. Raynaud, E. Champion, J.P. Lafon, D. Bernache-Assollant, Biomaterials 23 (2002) 1081–1089.
[29] S. Ramesh, C.Y. Tan, C.L. Peralta, W.D. Teng, Sci. Technol. Adv. Mater. 8 (2007) 257–263.